Case Studies in Thermal Engineering 76 (2025) 107415

Contents lists available at ScienceDirect

Case Studies in Thermal Engineering

journal homepage: www.elsevier.com/locate/csite

Geometrical optimization of shell and tube latent heat thermal energy storage reinforced by thermal fins- sintered copper wicks packages

Maher Jebali [a], Khalil Hajlaoui [b], Mohamed Bouzidi [c], Mansour Mohamed [c], Wahiba Yaïci [d], Nashmi H. Alrasheedi [b,*], Mohammad Ghalambaz [e,f,**], Pouyan Talebizadehsardari [g]

[a] Computer Science Department, Applied College, University of Ha'il, P.O. Box 2440, Hail City, 55476, Saudi Arabia
[b] College of Engineering, Imam Mohammad Ibn Saud Islamic University (IMSIU), Riyadh, Kingdom of Saudi Arabia
[c] Department of Physics, College of Science, University of Ha'il, P.O. Box 2440, Ha'il, Saudi Arabia
[d] CanmetENERGY Research Centre, Natural Resources Canada, 1 Haanel Drive, Ottawa, Ontario, Canada
[e] Department of Mathematical Sciences, Saveetha School of Engineering, SIMATS, Chennai, India
[f] Refrigeration and Air Conditioning Technical Engineering Department, College of Technical Engineering, The Islamic University, Najaf, Iraq
[g] Power Electronics, Machines and Control (PEMC) Institute, University of Nottingham, Nottingham, UK

GRAPHICAL ABSTRACT

A latent heat thermal energy storage unit with fins and copper wicks.

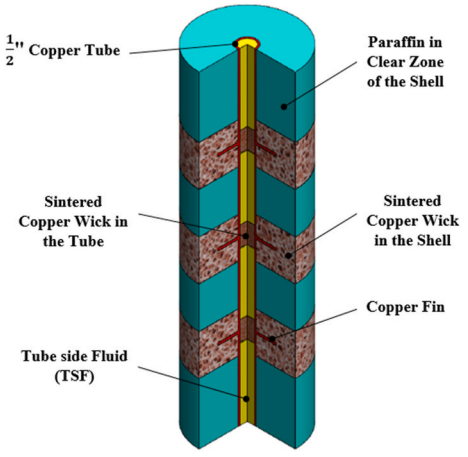

* Corresponding author.
** Corresponding author. Department of Mathematical Sciences, Saveetha School of Engineering, SIMATS, Chennai, India.
E-mail addresses: nhrasheedi@imamu.edu.sa (N.H. Alrasheedi), m.ghalambaz@gmail.com (M. Ghalambaz).

https://doi.org/10.1016/j.csite.2025.107415
Received 20 July 2025; Received in revised form 30 October 2025; Accepted 13 November 2025
Available online 14 November 2025

A R T I C L E I N F O

Keywords:
Finite element method
Local thermal non-equilibrium
Phase change materials (PCM)
Reinforced thermal fins- sintered copper wicks packages

A B S T R A C T

The current study aims to improve the thermal performance of a shell and tube latent heat thermal energy storage (LHTES) using packages of the thermal disk fins and the sintered Copper wicks. In an axis symmetric vertical model, the Paraffin wax, placed inside the shell, affected by the cold/hot Water flow crossing the central Copper tube, gets the phase change. The main focus is on the thermal disk fins covered by the sintered Copper wicks, where the best and the worst geometrical combinations can be found, leading to the maximum/minimum thermal performance of the LHTES, respectively. Once, the sets of partial differential equations (PDEs) within the Copper tube including the clear area and the sintered Copper wicks were declared. Once again, the PDEs covered the clear area and the sintered Copper wicks inside the shell. Intriguingly, the local thermal non-equilibrium (LTNE) conditions between the Water/PCM and the solid matrix of the sintered Copper wicks was also assumed. The calculated power and the needed time to complete melting/solidification modes were the substantial criteria to measure each case. The findings describe that the case including the Copper wicks spread on the Copper tube and the narrowest as well as the longest fins gets an improvement percentage in the power, over 38 %, in both the charging and the discharging modes against the initial designation. Moreover, using the thermal fins spread on the Copper tube can be equal a LHTES without any thermal fins.

Nomenclature

Latin	
A_{mush}	mushy constant value, 10^{10}, (Pa.s)/m^2
A_{sf}	Copper wick pore/TSF interface surface, 1/m
C_F	coefficient of Forchheimer, m
C_p	specific heat capacity, J/(kg.K)
d_{fp}	diameter of pore, m
d_{fs}	characteristic of pore, m
dV	volume element, m
e	constant of Copper wick structure, 0.339
E_s	constant value of mushy source term, 0.001
g	gravitational acceleration, m/s^2
H	height of shell, m
H_{fin}	fin height, m
$H_{CW,\ Shell}$	Copper wick height applied in the shell, m
$H_{CW,\ Tube}$	Copper wick height applied in the tube, m
h_{sf}	interface heat transfer, W/(m.K)
h_v	volumetric interface heat transfer W/(m^3.K)
k	thermal conductivity, W/(m.K)
L_f	latent heat of fusion, J/kg
M_A, M_B, M_C and M_D	dummy parameter, (m.K)/W
MVF	melting volume fraction
Nu_v	Nusselt number
P_o	pressure outlet, Pa
Pr	Prandtl number
r, z	coordinate system, m
Re	Reynolds number
R_{in}	inner radius of the Copper tube, in
R_{out}	outer radius of the Copper tube, in
t	time, s
T	Temperature, K
T_0	initial temperature, K
T_c	cold temperature, K
T_f	fusion temperature, K
T_h	hot temperature, K
T_{in}	inlet temperature, K
t_{Fin}	thickness of fin, m
t_{tube}	tube thickness, m
u	velocity component in r- direction, m/s
V	Volume, m^3
W_{Shell}	width of shell, m
$W_{CW,\ Shell}$	Copper wick width in the shell, m
w	velocity component in z-direction, m/s
Greek	
α	thermal diffusivity, m^2/s
β	coefficient of volumetric expansion, 1/K
ε	porosity inside the Copper wick
κ	permeability inside the Copper wick, m^2
κ_{tor}	pore flow Tortuosity

(*continued on next page*)

(*continued*)

μ	dynamic viscosity, Pa.s
μ_∞	artificial dynamic viscosity, 10^5 Pa s
ρ	density, kg/m^3
σ	dummy parameter
φ	melting fraction
Abbreviations	
imp	impressive
CW	Copper wick
LTNE	Local Thermal non- Equilibrium
PCM	phase change materials
TSF	tube side fluid

1. Introduction

Fins and porous media are both essential in heat transfer applications, significantly enhancing thermal performance in LHTES system; where using PCMs lonely cannot provide a sufficient efficiency within the referred systems. Fins increase the surface area for heat exchange, improving convective and conductive transfer in systems like heat exchangers and electronic cooling. Meanwhile, porous mediums offer high surface area and thermal conductivity, boosting fluid-solid interactions and ensuring efficient temperature regulation in cooling devices, reactors, and insulation materials. All in all, these elements play a critical role in advancing energy efficiency and effective thermal management across a wide range of engineering systems.

This section provides a structured review of the literature relevant to the proposed model. First, the influence of thermal fins and porous media—considering both Local Thermal Equilibrium (LTE) and Local Thermal Non-Equilibrium (LTNE) conditions—on the overall heat transfer rate is examined. Subsequently, the specific effects of these structures on Phase Change Materials (PCMs) are analyzed. Finally, Latent Heat Thermal Energy Storage (LHTES) units from the literature, which feature conditions and geometries similar to the present model, are reviewed.

Afzal et al. [1] provided a comprehensive review of steady and transient laminar conjugate heat transfer under forced convection conditions. Both their numerical and experimental findings emphasized that ignoring the conjugate nature of heat transfer, especially in complex geometries like finned surfaces, can result in significant inaccuracies when predicting thermal performance. In a numerical investigation, Gholami et al. [2] explored how using dimpled fins and different nanofluids can enhance natural convection heat transfer within a vertical channel. Their study emphasized the crucial role of the coupled interaction between the fluid flow and the solid fins. They found that adding fins not only increases the surface area for heat transfer but also alters the boundary layer dynamics, leading to more vigorous convective movements.

Sajjadi et al. [3] studied natural convection in a porous cavity filled with Cu/water nanofluid using a novel double multi-relaxation-time (MRT) lattice Boltzmann method. Their findings [3]showed that increasing porosity from 0.4 to 0.9 improved the Nusselt number by 10 %, 32 %, and 33 % for Rayleigh numbers of 10^3, 10^4, and 10^5, respectively. Liu et al. [4] applied digital rock technology to simulate pore-scale convective heat transfer inside a porous medium. Their results [4] highlighted that pore-level heterogeneities create spatial variations in heat transfer efficiency, particularly important for natural porous materials and engineered structures like metal foams. In another study, a self-organizing map neural network was used to analyze heat transfer in a porous ceramic matrix with internal heat generation [5]. The work [5] stood out by introducing an intelligent method to address the complex thermal behavior of porous systems. Chen et al. [6] examined natural convection in an open quadrilateral enclosure partially filled with porous media. They developed a new lattice Boltzmann model to handle fluid-porous interface challenges. Their analysis [6] showed that factors like porous layer thickness, thermal conductivity ratios, and permeability had significant—and sometimes surprising—impacts on heat transfer and flow patterns.

The local thermal non-equilibrium (LTNE) model is crucial in porous media heat transfer analysis as it accounts for temperature differences between fluid and solid phases. This model considers a temperature equation for the material in the pores and another temperature equation for the pore structure [7]. This enhances the accuracy of predicting thermal behavior, especially in systems with high heat flux or rapid flow, where traditional equilibrium models may significantly underestimate heat transfer performance. Jadhav et al. [8] investigated forced convection inside a horizontal pipe filled with aluminum metal foam using a two-dimensional numerical model based on the Darcy extended Forchheimer framework. They [8] applied the LTNE (local thermal non-equilibrium) model to capture detailed thermal interactions between the fluid and solid phases in the foam. Their study [8] effectively demonstrates how LTNE modeling can capture the critical impact of metallic porous media on local heat transfer performance. Cheng et al. [9] conducted pore-scale simulations of forced convection in packed beds made of uniform rough spheres, incorporating LTNE heat transfer mechanisms. The findings [9] emphasize the value of advanced LTNE formulations for accurately modeling heat transfer in realistic reactor setups, especially under conditions where flow patterns and thermal interactions are spatially nonuniform.

Phase change materials (PCMs) are widely used for thermal energy storage, temperature regulation, and passive cooling. They absorb, store, and release heat during phase transitions, making them valuable in applications like building insulation, solar energy systems, electronics cooling, textiles, and medical devices, enhancing energy efficiency and thermal management across industries. The numerical simulations have been an effective tool for modeling and design of phase change material. Esmonde [10] proposed an effective fractal topology and fractional calculus model phase transitions in materials through iterative, frequency-based analysis. Arıcı et al. [11] provided a detailed numerical investigation examined how boundary conditions affect natural convection heat transfer in molten PCMs within confined geometries. The results [11] highlighted the critical role of selecting appropriate boundary conditions

when modeling PCM-based thermal systems, especially under convective conditions. To improve energy storage in solar cooking, an experimental study introduced a hot box cooker using Paraffin wax as the PCM, housed in vertically positioned capsule-shaped units above a cooking tray [12]. The findings [12] show that combining PCM with extended surface geometry offers an efficient, cost-effective solution for off-grid or remote solar cooking applications. Chu et al. [13] numerically assessed ways to accelerate PCM solidification using two passive strategies: adopting a wavy enclosure shape and adding Copper oxide nanoparticles (0.04 concentration). Their results [13] showed that both enclosure shape and wall waviness notably reduced solidification time to 156.17s. A numerical study on the melting behavior of lauric acid (PCM) around a horizontal cylinder in a square cavity showed how cylinder placement affects heat transfer [14]. Using the enthalpy–porosity method, six-cylinder positions were analyzed, revealing that as the cylinder is raised from the cavity base, both convective heat transfer and melt fraction decrease. Labihi et al. [15] investigated the integration of PCM layers into wall structures to boost natural convection, combining numerical modeling and experimental testing within a differentially heated, air-filled enclosure. Notably, experimental results diverged from initial models that omitted density variations during solidification, underscoring the importance of accurately incorporating material properties and phase change dynamics in PCM system simulations.

The non-Newtonian effects of a power-law PCM were investigated in Ref. [16]. Effect of the thermal fin numbers was also evaluated. An increase in the power-law index indicates a longer charging time for the storage system, whereas adding solid fins—from one to three—helps shorten the charging duration. Zayed et al. [17] conducted an extensive review on the design of PCM containers, underscoring the ongoing issue of low thermal conductivity in phase change materials, which limits energy transfer rates in thermal energy storage (TES) systems. Their comparative analysis [17] further showed that using fins alone was more effective for heat transfer enhancement than combining fins with nanoparticles. In a focused numerical study, Tian et al. [18] examined how the material of fins impacts PCM melting behavior inside a rectangular enclosure, assessing metrics such as melting duration, stored energy, and cost efficiency. The introduction of fins significantly reduced melting time—by 41.6 %, 41.0 %, 40.1 %, and 37.2 % for Copper, aluminum, carbon steel, and steel302 fins, respectively, compared to systems without fins. Kalbasi et al. [19] analyzed the optimal number of fins for PCM-based heat sinks, particularly under conditions relevant to electronics cooling. Through a broad parametric study covering over 900 heat sink designs, they mapped the relationship between heat sink height (10–30 mm) and fin thickness (0.2–0.5 mm). Their findings [19] indicated that thicker fins typically required fewer units for optimal performance, while taller heat sinks benefited from wider spacing and thus fewer fins to maintain efficiency. Experimental and numerical analyses on the performance of heat transfer fins in TES systems highlighted the critical role of fin surface area during both the melting and solidification phases [20]. A specially engineered fin geometry achieved a striking 65 % reduction in melting time, underscoring that tailored fin shapes are more effective than simply enlarging surface area. Kok [21], in a numerical investigation, assessed both PCM and Nano-PCM systems using innovative fin designs to overcome the problem of unmelted regions often found in TES units. Without any fins, full melting was unachievable, especially in Nano-PCM, where only 36 % melted after 120 min. The introduction of a new fin configuration enhanced PCM melting time by 63 %, demonstrating the significant influence of geometry on thermal performance.

Ghalambaz and Zhang [22] conducted a numerical investigation into the performance of PCM combined with metal foams in a heatsink. Using the enthalpy-porosity approach along with the Darcy-Brinkman model, they [22] analyzed a setup where PCM-metal foam was packed between two concentric plates. Their findings [22] showed that when the Biot number is below 0.2, the integration of PCM and metal foam significantly improved thermal control. Chen et al. [23] studied a vertical rectangular cavity filled with lauric acid PCM, outfitted with triangular double fins, and evaluated the effects of adding nanoparticles, porous medium, and their combinations. They [23] discovered while the use of porous medium alone substantially boosted melting performance, combining porous structures with nanoparticles actually worsened results, suggesting that hybrid systems require careful optimization. Nematpourkeshteli et al. [24] carried out a comparative numerical analysis aiming to boost PCM thermal conductivity in a triplex-tube heat exchanger (TTHX). They tested different enhancement methods, including metal foams, nanoparticles, and fins, using organic PCMs with varying melting points in the central section, while heat transfer fluid moved through the inner and outer tubes. Their results [24] showed that using metal foams with porosities between 0.98 and 0.92 accelerated melting dramatically, cutting melting time by up to 69.52 % compared to plain PCM. When fins were added, the system achieved even greater performance, shortening melting time by 53.17 % relative to the nanoparticle-only setup. In a transient CFD study by Khanlari et al. [25], the use of porous fins to improve the performance of a PCM-enhanced solar air collector has been explored. Paraffin wax served as the PCM, and six configurations were compared: one without PCM and five incorporating porous fins on the bottom side of the absorber plate. Adding the PCM unit alone increased the collector's operational duration, while the inclusion of porous fins further raised the melting rate and overall system efficiency. As the number of fins increased, so did thermal efficiency, rising from 38.66 % to 41.73 %.

Latent Heat Thermal Energy Storage (LHTES) systems are widely used for efficient energy management in applications like solar power, building heating and cooling, industrial waste heat recovery, and electronic device thermal regulation. By storing and releasing large amounts of heat during phase change, LHTES enhances energy efficiency, reduces peak loads, and lowers operational costs. Using the enthalpy–porosity method, Ranga et al. [26] examined how fin shape, spacing, and PCM properties affect thermal performance in LHTES under both conduction and convection modes. Under natural convection, they [26] found that Hexagonal fins outperformed rectangular ones, improving melting by 18 % and storage efficiency by 12 %. Cao et al. [27] evaluated heat and fluid flow characteristics in LHTES systems utilizing a PCM tank, focusing on how porous media and NEPCM (nano-enhanced PCM) concentrations affect heat flux across the phase change zone. Their results [27] showed that combining NEPCM-enhanced fluids with porous materials can significantly boost system efficiency. Passaro et al. [28] assessed a multi-pass finned tube heat exchanger integrated into an LHTES system, examining how fins and nanoparticles together influence discharge performance. Simulations revealed that reducing fin pitch improved the heat transfer fluid (HTF) outlet temperature and led to more uniform phase change. In a spherical LHTES setup, Amini and Hekmat [29] explored improving thermal performance by combining innovative fin shapes with metal foam as a porous medium.

They [29] tested three fin types and metal foam porosities, comparing them to a finless system. Seven evenly spaced fins reduced melting and solidification times by 58.76 % and 72.66 %, respectively, while adding 85 % porosity metal foam slashed these times by an impressive 89.11 % and 94.96 %. A horizontal LHTES system using porous fins was studied in Ref. [30] to tackle PCM's low thermal conductivity. Analyzing eight fin designs across varying porosity levels and Darcy numbers, the research found that porous fins enhanced buoyancy-driven flow, dramatically speeding up melting. At optimal conditions (70 % porosity, four full-scale porous fins), complete melting time dropped by 46.4 % compared to solid fins, and stored energy rose by 19.6 %. Mozaffari et al. [31] investigated boosting LHTES performance by enhancing PCM thermal behavior using anisotropic metal foams (AMFs). Through computational models, they [31] tested 12 funnel-shaped AMF layer (AMFL) setups with varying placement, coverage, and orientation to maximize heat transfer and melting. They [31] found that placing larger AMFLs near the hot wall increased the melting rate, and raising AMFL coverage from 36 % to 60 % improved efficiency by about 3.1 %.

The influence of geometry on the performance of Latent Heat Thermal Energy Storage (LHTES) units has been extensively reviewed in the literature. Both thermal fins and porous media, have been shown to significantly enhance overall performance, either individually or in combination. The objective of this study is to identify the optimal and least effective geometrical configurations of thermal fins and sintered Copper wick structures within the proposed LHTES unit. Meanwhile, as reviewed, none of the valid papers conducted such a global geometrical optimization.

2. Physical model justification

Fig. 1 reveal the cylindrical LHTES which is symmetrical than z-axis. The partially-sintered Copper tube with a nominal diameter of $D_{Nominal\text{-}Tube} = \frac{1}{2}\ in$ and thickness of $0.049in$ has been placed in the center of LHTES. Moreover, three thermal disk fins have been mounted on the outer wall of the tube. In order to improve the heat transfer rate. We made a decision to reinforce the thermal disk fins by applying the sintered copper wicks, as depicted in Fig. 1. In our initial designation, length of the disk fins and the copper wicks inside the shell are considered to be 1.5 and 3.5 times larger than nominal diameter of the tube ($D_{Nominal\text{-}Tube}$). About the thickness of both the fins and the sintered copper wicks in the shell, since the constant occupied volume by the disk fins and the mentioned sintered Copper wicks is envisaged, inevitably, the thickness is directly depended on the related length and volume. Worthy to note that the disk fin and the referred metal wicks occupy $V_{fin} = 4.42\ cm^3$ and $V_{mf\text{-}\ shell} = 224.53\ cm^3$ inside the shell, respectively. Moreover, the overall dimension of the shell can be referred as $3.5 \times D_{Nominal\text{-}Tube}$ in diameter and $24 \times D_{Nominal\text{-}Tube}$ in height.

The tube side contains pure Water steadily entering from its bottom side by a specified inlet velocity. On the contrary, the shell is saturated by pure Paraffin wax as a matter which gets a proper phase change via a small temperature variation. There have been two distinct scenarios for the phase change process: the first one is that the tube and the shell have been selected as hot and cold sides, respectively. Actually, the high temperature Water flows inside the tube from the bottom side. Hence, due to the high thermal conductivity of copper ($k = 400$W/m.K), tube wall, the thermal fins and finally the sintered Copper wicks placed inside the shell get hot; consequently, a phase change for fully solid Paraffin wax will be expected. The second scenario happens in the reverse direction of heat transfer said in the first scenario. Indeed, the tube as the cold side includes the low temperature Water and in the same time, Paraffin wax is initially fully molten. In accordance to the reason described for the first scenario, hereon, Paraffin wax takes the cold from crossing Water so that solidification process can be reached in this case.

Important to note that local thermal non-equilibrium (LTNE) between PCM and the sintered Copper wicks in the shell as well as Water and the sintered Copper wicks in the tube has been taken into the account. Despite of the fact that Water gets laminar forced

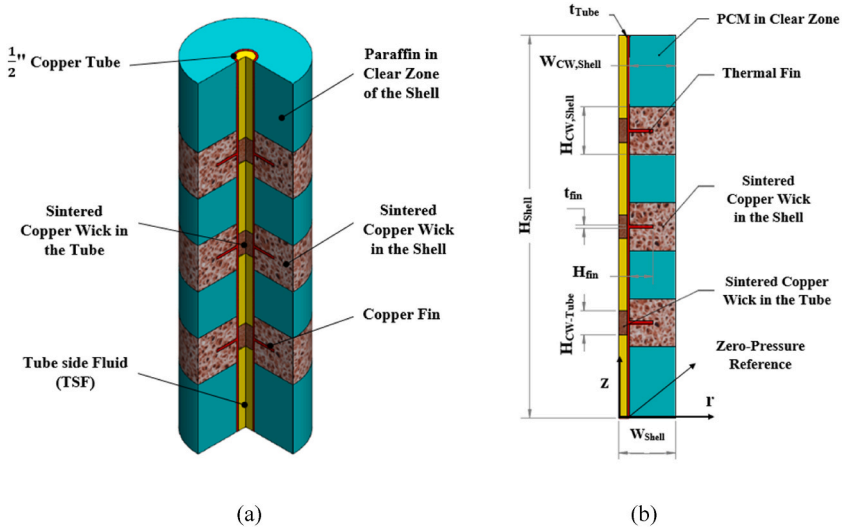

Fig. 1. Physical model designation (a) 3D view, and (b) 2D in details.

convection via a specified inlet velocity, laminar natural convection assigns to the molten Paraffin wax. Thus, the well-known Boussinesq's approximation would also be validated inside the shell. In addition, any slip on the inner wall of the tube on behalf of crossing Water is trivial.

The thermophysical properties of all the materials applied in the present study including Paraffin wax, Water and Copper have been collected in Table 1. Since Paraffin wax has phase change in the shell side, the mentioned properties have properly been provided both molten and solid phases. Transfer between the dual values in the phase change process has some principles which are extended in Governing Equation and Numerical Approach sections. It is while Water single phase fluid and Copper have constant values as shown in the referred table.

3. Governing equations build up

Dependent on the descriptions and assumptions provided in the previous part, physical model justification, the governing equations in the present study have been categorized in four main groups. Since the tube side and the shell side contain both clear and Copper wick, two ones belong to the tube side and two others to the shell side. Forced and natural convection heat transfer are common modes in the tube and the shell sides, respectively. Anyway, all the appeared equations hereon, are placed beneath the partial differential equations (PDEs). In more precise terms, the continuity, the momentum (in r and z directions), and the thermal (energy) equations take part in each one of the related zones in the cylindrical coordination. Importantly, to show the governing equations groups, a direction from the tube side zones to the shell one has been considered. The complementary explanations over the groups have been provided before each one.

The first group includes Equations (1)–(4) for the clear zone of the tube side; so that Equation (1), Continuity, Equations (2) and (3), r and z components of Momentum, and finally, Equation (4) thermal (energy) which are steady state in the mentioned zone:

$$\frac{1}{r}\frac{\partial\left(ru_{r,TSF}\right)}{\partial r}+\frac{\partial u_{z,TSF}}{\partial z}=0 \tag{1}$$

$$\rho_{\mathrm{TSF}}\left(u_{z,TSF}\frac{\partial u_{r,TSF}}{\partial z}+u_{r,TSF}\frac{\partial u_{r,TSF}}{\partial r}\right)=-\frac{\partial p}{\partial r}+\frac{\mu_{\mathrm{TSF}}}{r}\frac{\partial}{\partial r}\left(r\frac{\partial u_{r,TSF}}{\partial r}\right)+\mu_{\mathrm{TSF}}\frac{\partial^2 u_{r,TSF}}{\partial z^2}-\frac{\mu_{\mathrm{TSF}}u_{r,TSF}}{r^2} \tag{2}$$

$$\rho_{\mathrm{TSF}}\left(u_{z,TSF}\frac{\partial u_{z,TSF}}{\partial z}+u_{r,TSF}\frac{\partial u_{z,TSF}}{\partial r}\right)=-\frac{\partial p}{\partial z}+\frac{\mu_{\mathrm{TSF}}}{r}\frac{\partial}{\partial r}\left(r\frac{\partial u_{z,TSF}}{\partial r}\right)+\mu_{\mathrm{TSF}}\frac{\partial^2 u_{z,TSF}}{\partial z^2} \tag{3}$$

$$\left(\rho C_p\right)_{\mathrm{TSF}}\left(u_{z,TSF}\frac{\partial T_{TSF}}{\partial z}+u_{r,TSF}\frac{\partial T_{TSF}}{\partial r}\right)=k_{\mathrm{TSF}}\left(\frac{1}{r}\frac{\partial}{\partial r}\left(r\frac{\partial T_{TSF}}{\partial r}\right)+\frac{\partial^2 T_{TSF}}{\partial z^2}\right) \tag{4}$$

The second group of the governing equations have been introduced in the tube side Copper wicks. Hence, Except of Equation (5), the continuity of Water fluid in the wicks, the others have gotten some changes than Equations (2)–(4). To distinguish Momentum equations in the Copper wicks, the most complete scheme, Darcy–Brinkman–Forchheimer flow model, has been chosen. Around the energy equation, on behalf of the local thermal non equilibrium (LTNE) conditions between the fluid and Copper wick, the thermal (energy) equation itself divides in two distinct equations. They are related to each other via the interfaces which are introduced as follow:

$$\frac{1}{r}\frac{\partial\left(ru_{r,TSF}\right)}{\partial r}+\frac{\partial u_{z,TSF}}{\partial z}=0 \tag{5}$$

$$\frac{\rho_{\mathrm{TSF}}}{\varepsilon^2}\left(u_{z,TSF}\frac{\partial u_{r,TSF}}{\partial z}+u_{r,TSF}\frac{\partial u_{r,TSF}}{\partial r}\right)=-\frac{\partial p}{\partial r}+\frac{\mu_{\mathrm{TSF}}}{\varepsilon}\left(\frac{1}{r}\frac{\partial}{\partial r}\left(r\frac{\partial u_{r,TSF}}{\partial r}\right)-\frac{u_{r,TSF}}{r^2}+\frac{\partial^2 u_{r,TSF}}{\partial z^2}\right)-\rho_{\mathrm{TSF}}\frac{C_F}{\sqrt{\kappa}}\left|u_{TSF}\right|u_{r,TSF}-\frac{\mu_{\mathrm{TSF}}}{\kappa}u_{r,TSF} \tag{6}$$

Table 1
The thermophysical characteristics of the matters utilized in the present study.

Materials	ρ (kg/m^3)	k (W/m.K)	C_p (J/kg.K)	L (kJ/kg)	T_m (°C)	μ (kg/m.s)	β (1/K)
Paraffin wax [32–34]	916/790	0.21/0.12	2700/2900	176	49–54	36×10^{-4}	91×10^{-5}
Water [35]	997.1	0.613	4179	–	–	95.7×10^{-5}	21×10^{-5}
Copper wick/Tube Wall [36]	8900	380	386	–	–	–	–

$$\frac{\rho_{\mathrm{TSF}}}{\varepsilon^2}\left(u_{z,TSF}\frac{\partial u_{z,TSF}}{\partial z}+u_{r,TSF}\frac{\partial u_{z,TSF}}{\partial r}\right)=-\frac{\partial p}{\partial z}+ \\ \frac{\mu_{\mathrm{TSF}}}{\varepsilon}\left[\frac{\partial^2 u_{z,TSF}}{\partial z^2}+\frac{1}{r}\frac{\partial}{\partial r}\left(r\frac{\partial u_{z,TSF}}{\partial z}\right)\right]-\rho_{\mathrm{TSF}}\frac{C_F}{\sqrt{\kappa}}|u_{TSF}|u_{z,TSF}-\frac{\mu_{\mathrm{TSF}}}{\kappa}u_{z,TSF} \tag{7}$$

$$(\rho C_p)_{\mathrm{TSF}}\left(u_{z,TSF}\frac{\partial T_{\mathrm{TSF}}}{\partial z}+u_{r,TSF}\frac{\partial T_{\mathrm{TSF}}}{\partial r}\right)=\frac{1}{r}\frac{\partial}{\partial r}\left(k_{\mathrm{Imp,TSF}}r\frac{\partial T_{TSF}}{\partial r}\right)+ \\ \frac{\partial}{\partial z}\left(k_{\mathrm{Imp,TSF}}\frac{\partial T_{HTF}}{\partial z}\right)+h_{\mathrm{sf}}A_{\mathrm{sf}}(T_{\mathrm{CW}}-T_{\mathrm{TSF}}) \tag{8}$$

$$0=\frac{1}{r}\frac{\partial}{\partial r}\left(k_{\mathrm{Imp-CW}}r\frac{\partial T_{\mathrm{MF}}}{\partial r}\right)+\frac{\partial}{\partial z}\left(k_{\mathrm{Imp-CW}}\frac{\partial T_{\mathrm{CW}}}{\partial z}\right)+h_{\mathrm{sf}}A_{\mathrm{sf}}(T_{\mathrm{TSF}}-T_{\mathrm{CW}}) \tag{9}$$

In Equations (6) and (7), the second, third and fourth terms in the right side of the equations explain Brinkman, Frochheimer, and Darcy terms in their bodies. C_{F} is also drag coefficient raising from Frochheimer term [37] which is given by:

$$C_{\mathrm{F}}=0.00212\times\left(\frac{d_{\mathrm{fs}}}{d_{\mathrm{fp}}}\right)^{-1.63}(1-\varepsilon)^{-0.132},d_{\mathrm{fp}}=2.54\times10^{-2}\Big/PPI,d_{\mathrm{fs}}=1.18\left\{\frac{1}{1-e^{\frac{(\varepsilon-1)}{0.04}}}\right\}\sqrt{\frac{(1-\varepsilon)}{3\pi}}d_{\mathrm{fp}} \tag{10}$$

Moreover, d_{fp} and d_{fs} show void diameter and void characteristic in Copper wick [37]. Another parameter appeared in the above equations is permeability (κ) [38,39]

$$\kappa=\frac{\varepsilon^2}{36}\frac{\left(\sqrt{\frac{\kappa_{\mathrm{tor}}}{3\varepsilon}}d_{fp}\right)^2}{\kappa_{\mathrm{tor}}(\kappa_{\mathrm{tor}}-1)} \tag{11}$$

In the current study, effect of the void flow tortuosity (κ_{tor}) in Copper wick has been taken into account and established as [37]:

$$\frac{1}{\kappa_{\mathrm{tor}}}=\frac{1}{\varepsilon}\left(\frac{3}{4}+\frac{\sqrt{9-8\varepsilon}}{2}\times\cos\left(\frac{4}{3}\pi+\frac{1}{3}\cos^{-1}\left(\frac{8\varepsilon^2+27-36\varepsilon}{(9-8\varepsilon)^{\frac{3}{2}}}\right)\right)\right) \tag{12}$$

Interface surface between TSF and Copper wick void is also specified [40–43]:

$$A_{\mathrm{sf}}=\frac{3\pi\left(1-e^{-\frac{(1-\varepsilon)}{0.004}}\right)d_{\mathrm{fs}}}{0.59d_{\mathrm{fp}}} \tag{13}$$

Thermal diffusivity of TSF inside the related Copper wicks can be demonstrated in the below equation:

$$\alpha_{\mathrm{TSF}}=\frac{k_{\mathrm{TSF}}}{(\rho C_p)_{\mathrm{TSF}}} \tag{14}$$

in TSF domain, the impressive thermal conductivity of TSF and Copper wick [38–40,44] is specified through:

$$k_{\mathrm{Imp,TSF/CW}}=\frac{\sqrt{2}}{2(M_{\mathrm{I}}+M_{\mathrm{II}}+M_{\mathrm{III}}+M_{\mathrm{IV}})} \tag{15}$$

$$M_{\mathrm{I}}=\frac{4\sigma}{((2e^2+\pi\kappa(1-e))k_{\mathrm{CW}}+(4-2e^2-\pi\sigma(1-e))k_{\mathrm{TSF}})} \tag{16}$$

$$M_{\mathrm{II}}=\frac{(\varepsilon-2\sigma)^2}{((e-2\sigma)e^2k_{\mathrm{CW}}+(2e-4\sigma-e^2(e-2\sigma))k_{\mathrm{TSF}})} \tag{17}$$

$$M_{III}=\frac{\left(\sqrt{2}-2\sigma\right)^2}{\left(2\pi\sigma^2\left(1-2\sqrt{2}\ e\right)k_{\mathrm{CW}}+2\left(\sqrt{2}-2e-\pi\sigma^2\left(1-2\sqrt{2}\ e\right)\right)k_{\mathrm{TSF}}\right)} \tag{18}$$

$$M_{\mathrm{IV}}=\frac{2e}{(e^2k_{\mathrm{CW}}+(4-e^2)k_{\mathrm{TSF}})} \tag{19}$$

$$\sigma=\sqrt{\frac{\sqrt{2}\left(2-\frac{5}{8}\sqrt{2}\ e^3-2\varepsilon\right)}{\left(\pi(3-4\sqrt{2}\ e-e)\right)}},e=0.339 \tag{20}$$

in the case of $k_{\mathrm{Imp,\ CW}}$ is considered, zero value belongs to $k_{\mathrm{Imp,\ TSF}}$ in Equation (16)–(19). Reversely, to reach $k_{\mathrm{Imp,\ TSF}}$ in Equation (15), $k_{\mathrm{Imp,\ CW}}$ should tend to zero value in the mentioned equations.

Interface heat transfer between TSF and Copper wick in tube side is expressed as follow [40,41]:

$$h_{\mathrm{sf}}=Nu_{\mathrm{sf}}\frac{k_{\mathrm{sf}}}{d_{\mathrm{fp}}} \tag{21}$$

in the above equation, Nusselt number regarding TSF in the Copper wick can be introduced as below [40,41]:

$$Nu_{\mathrm{sf}}=\begin{cases}0.76\mathrm{Pr}_{TS-CW}^{0.37}\mathrm{Re}_{\mathrm{TS-CW}}^{0.4},1\le\mathrm{Re}_{\mathrm{TS-CW}}\le40\\0.52\mathrm{Pr}_{TS-CW}^{0.37}\mathrm{Re}_{\mathrm{TS-CW}}^{0.5},40\le\mathrm{Re}_{\mathrm{TS-CW}}\le1000\\0.26\mathrm{Pr}_{TS-CW}^{0.37}\mathrm{Re}_{\mathrm{TS-CW}}^{0.6},1000\le\mathrm{Re}_{\mathrm{TS-CW}}\le10^5\end{cases} \tag{22}$$

where $\mathrm{Pr}_{\mathrm{TS\text{-}CW}}$ and $\mathrm{Re}_{\mathrm{TS\text{-}CW}}$ explain Prandtl and void scale Rayleigh numbers in tube side Copper wick, respectively:

$$\mathrm{Pr}=\frac{\mu_{\mathrm{TSF}}\rho_{\mathrm{TSF}}}{\alpha_{\mathrm{TSF}}},\mathrm{Re}_{\mathrm{TS,CW}}=\frac{\rho_{\mathrm{TSF}}d_{\mathrm{sp}}u_{\mathrm{TSF}}}{\mu_{\mathrm{TSF}}} \tag{23}$$

The inner zone of the tube and the shell zone have been separated via the tube wall with the specified matter and thickness. Hence, the conjugate heat transfer nearby the tube wall can be expected. So, as a thermal bridge between the tube side and the shell side, thermal (energy) equation in the tube wall can be given by:

$$\left(\rho C_p\right)_{\mathrm{TW}}\frac{\partial T}{\partial t}=k_{\mathrm{TW}}\left(\frac{\partial^2T}{\partial z^2}+\frac{1}{r}\frac{\partial}{\partial r}\left(r\frac{\partial T}{\partial r}\right)\right) \tag{24}$$

Hereon, the governing equations in clear zone of the shell side have been appointed. Equation (25) is introduced for the liquid PCM. Despite of water in the tube side, phase change process for Paraffin wax happens as long as cold/hot Water is current inside the tube side. Thus, Equations (26) and (27) for r and z components of the Momentum equations contain phase change term in their bodies versus Equations (2) and (3) which are provided for Water single phase fluid. In addition, because of natural convection heat transfer, the term regarding buoyancy forces is appeared in z-component of the Momentum equation. Equation (28) shows thermal (energy) one for the PCM. As seen, phase change effect has been provided via the last term placed in the right side of the equation, a term which is affected by the PCM latent heat fusion.

$$\frac{1}{r}\frac{\partial\left(ru_{r,PCM}\right)}{\partial r}+\frac{\partial u_{z,PCM}}{\partial z}=0 \tag{25}$$

$$\rho_{\mathrm{PCM}}\left(\frac{\partial u_{r,PCM}}{\partial t}+u_{z,PCM}\frac{\partial u_{r,PCM}}{\partial z}+u_{r,PCM}\frac{\partial u_{r,PCM}}{\partial r}\right)=-\frac{\partial p}{\partial r}+A_{mush}\frac{(1-\varphi(T))^2}{\lambda_{mush}+\varphi^3(T)}u_{r,PCM}+\\\frac{\mu_{\mathrm{PCM}}}{r}\frac{\partial}{\partial r}\left(r\frac{\partial u_{r,PCM}}{\partial r}\right)+\mu_{\mathrm{PCM}}\frac{\partial^2u_{r,PCM}}{\partial z^2}-\frac{\mu_{\mathrm{PCM}}u_{r,PCM}}{r^2} \tag{26}$$

$$\rho_{\mathrm{PCM}}\left(\frac{\partial u_{z,PCM}}{\partial t}+u_{z,PCM}\frac{\partial u_{z,PCM}}{\partial z}+u_{r,PCM}\frac{\partial u_{z,PCM}}{\partial r}\right)=-\frac{\partial p}{\partial z}+A_{mush}\frac{(1-\varphi(T))^2}{\lambda_{mush}+\varphi^3(T)}u_{z,PCM}+\\\frac{\mu_{\mathrm{PCM}}}{r}\frac{\partial}{\partial r}\left(r\frac{\partial u_{z,PCM}}{\partial r}\right)+\mu_{\mathrm{PCM}}\frac{\partial^2u_{z,PCM}}{\partial z^2}+g\rho_{\mathrm{PCM}}\beta_{\mathrm{PCM}}(T-T_0) \tag{27}$$

$$\left(\rho C_p\right)_{\mathrm{PCM}}\left(\frac{\partial T_{PCM}}{\partial t}+u_{z,PCM}\frac{\partial T_{PCM}}{\partial z}+u_{r,PCM}\frac{\partial T_{PCM}}{\partial r}\right)=\\k_{\mathrm{PCM}}\left(\frac{1}{r}\frac{\partial}{\partial r}\left(r\frac{\partial T_{PCM}}{\partial r}\right)+\frac{\partial^2T_{PCM}}{\partial z^2}\right)-\rho_{PCM}L_{f,PCM}\frac{\partial\varphi(T_{PCM})}{\partial t} \tag{28}$$

Melting/solidification conditions depicted in the above equations can be specified via Equation (29):

$$\varphi(T_{PCM})=\begin{cases}0 & T_{PCM}<\left(T_{\text{fluid}}-\frac{1}{2}\Delta T_{\text{fluid}}\right)\\ \frac{1}{2}+\frac{(T_{PCM}-T_{\text{fluid}})}{\Delta T_{\text{fluid}}} & \left(T_{\text{fluid}}-\frac{1}{2}\Delta T_{\text{fluid}}\right)\le T_{PCM}\le\left(T_{\text{fluid}}+\frac{1}{2}\Delta T\right)_{\text{fluid}}\\ 1 & T_{PCM}>\left(T_{\text{fluid}}+\frac{1}{2}\Delta T_{\text{fluid}}\right)\end{cases} \tag{29}$$

A description of the PCM heat capacity has been appeared in equation (30):

$$(\rho C_p)_{\text{PCM}}=\varphi(\rho C_p)_{\text{solid}}+(1-\varphi)(\rho C_p)_{\text{liquid}} \tag{30}$$

in the same way,

$$\rho_{\text{PCM}}=\varphi\rho_{\text{solid}}+(1-\varphi)\rho_{\text{liquid}} \tag{31}$$

Governing Equations in the shell side Copper wicks have been illustrated in Equations (32)–(36). As mentioned so far, Continuity of the liquid PCM is common inside the Copper wicks. Brinkman- Darcy flow model is valid in the Momentum components while Forchheimer aspect can be down due to the governed natural convection heat transfer in the shell side. Also, twin Equations (35) and (36) are provided since local thermal non-equilibrium (LTNE) has been considered for the PCM and Copper wick.

$$\frac{1}{r}\frac{\partial(ru_{r,PCM})}{\partial r}+\frac{\partial u_{z,PCM}}{\partial z}=0 \tag{32}$$

$$\begin{aligned}&\frac{\rho_{\text{PCM}}}{\varepsilon}\left(\frac{\partial u_{r,PCM}}{\partial t}+\frac{1}{\varepsilon}\left(u_{z,PCM}\frac{\partial u_{r,PCM}}{\partial z}+u_{r,PCM}\frac{\partial u_{r,PCM}}{\partial r}\right)\right)=-\frac{\partial p}{\partial r}+\\ &A_{mush}\frac{(1-\varphi(T))^2}{\lambda_{mush}+\varphi^3(T)}u_{r,PCM}+\frac{\mu_{\text{PCM}}}{\varepsilon}\left[\frac{1}{r}\frac{\partial}{\partial r}\left(r\frac{\partial u_{r,PCM}}{\partial r}\right)-\frac{u_{r,PCM}}{r^2}+\frac{\partial^2 u_{r,PCM}}{\partial z^2}\right]-\frac{\mu_{\text{PCM}}}{\kappa}u_{r,PCM}\end{aligned} \tag{33}$$

$$\begin{aligned}&\frac{\rho_{\text{PCM}}}{\varepsilon}\left(\frac{\partial u_{z,PCM}}{\partial t}+\frac{1}{\varepsilon}\left(u_{z,PCM}\frac{\partial u_{z,PCM}}{\partial z}+u_{r,PCM}\frac{\partial u_{z,PCM}}{\partial r}\right)\right)=-\frac{\partial p}{\partial z}+\\ &A_{mush}\frac{(1-\varphi(T))^2}{\lambda_{mush}+\varphi^3(T)}u_{z,PCM}+\frac{\mu_{\text{PCM}}}{\varepsilon}\left[\frac{\partial^2 u_{z,PCM}}{\partial z^2}+\frac{1}{r}\frac{\partial}{\partial r}\left(r\frac{\partial u_{z,PCM}}{\partial z}\right)\right]-\frac{\mu_{\text{PCM}}}{\kappa}u_z+\\ &g\rho_{\text{PCM}}\beta_{\text{PCM}}(T-T_0)\end{aligned} \tag{34}$$

$$\begin{aligned}&(\rho C_p)_{\text{PCM}}\left(\varepsilon\frac{\partial T_{\text{PCM}}}{\partial t}+\left(u_z\frac{\partial T_{\text{PCM}}}{\partial z}+u_r\frac{\partial T_{\text{PCM}}}{\partial r}\right)\right)=\frac{1}{r}\frac{\partial}{\partial r}\left(k_{\text{Imp-SS-CW}}r\frac{\partial T_{\text{PCM}}}{\partial r}\right)+\\ &\frac{\partial}{\partial z}\left(k_{\text{Imp-SS-CW}}\frac{\partial T_{\text{PCM}}}{\partial z}\right)-\varepsilon\rho_{\text{PCM}}L_{\text{PCM}}\frac{\partial\varphi(T)}{\partial t}+h_v(T_{\text{CW}}-T_{\text{PCM}})\end{aligned} \tag{35}$$

$$\begin{aligned}&(\rho C_p)_{\text{CW}}(1-\varepsilon)\frac{\partial T_{\text{CW}}}{\partial t}=\frac{1}{r}\frac{\partial}{\partial r}\left(k_{\text{Imp-SS-CW}}r\frac{\partial T_{\text{CW}}}{\partial r}\right)+\frac{\partial}{\partial z}\left(k_{\text{Imp-SS-CW}}\frac{\partial T_{\text{CW}}}{\partial z}\right)+\\ &h_v(T_{\text{PCM}}-T_{\text{CW}})\end{aligned} \tag{36}$$

in addition, α_{PCM} describes thermal diffusivity of PCM:

$$\alpha_{\text{PCM}}=\frac{k_{\text{PCM}}}{(\rho C_p)_{\text{PCM}}} \tag{37}$$

Impressive thermal conductivity of Copper wick and PCM in the shell side are shown in equations (17) and (18), respectively [38, 39]:

$$k_{\text{Imp-SS-CW}}=\frac{(1-\varepsilon)}{3}k_{\text{SS-CW-PCM}} \tag{38}$$

$$k_{\text{Imp,PCM}}=k_{\text{PCM}}\frac{\varepsilon+2}{3} \tag{39}$$

Equation (40) depicts volumetric form of interface heat transfer between Copper wick and PCM in shell side [43]:

$$h_v=\frac{k_{\text{PCM}}}{d_{\text{fs}}^2}Nu_v \tag{40}$$

and the related PCM Nusselt number in the Copper wick can be written as:

$$Nu_v = \begin{cases} (76.99 - 152.01 \times \varepsilon + 75.04 \times \varepsilon^2), 0 \le \mathrm{Re}_{\mathrm{SS-CW}} \le 0.1 \\ (1.72 + 1.71 \times \varepsilon - 3.46 \times \varepsilon^2) \times \mathrm{Re}^{0.26} \times \mathrm{Pr}^{0.28}, 0.1 < \mathrm{Re}_{\mathrm{SS-CW}} \le 1 \end{cases} \quad (41)$$

Void scale Reynolds number ($\mathrm{Re}_{\mathrm{SS\text{-}CW}}$) and Prandtl number ($\mathrm{Pr}_{\mathrm{SS\text{-}CW}}$) in shell side Copper wick are expressed as:

$$\mathrm{Re}_{\mathrm{SS-CW}} = \frac{\rho_{\mathrm{PCM}} d_{\mathrm{fs}} u_{\mathrm{PCM}}}{\mu_{\mathrm{PCM}}}, \mathrm{Pr}_{\mathrm{SS-CW}} = \frac{\mu_{\mathrm{PCM}} \rho_{\mathrm{PCM}}}{\alpha_{\mathrm{PCM}}} \quad (42)$$

3.1. Model boundary and initial conditions

In accordance to two scenarios introduced in the previous section, Physical Model Justification, the initial and the boundary conditions have been provided.

The first scenario says that hot inlet water/cold solid Paraffin wax. So, initial temperature of the shell side becomes:

$$T|_{Initial,SS} = T_c \quad (43)$$

On the contrary, the second scenario specifies cold inlet Water/hot molten Paraffin wax:

$$T|_{Initial,SS} = T_h \quad (44)$$

As an important boundary condition, hot/cold Water which does not bring any pressure gauge from its source, gets the inlet velocity (U_{in}) at the entrance of the tube side. In addition, the pressure outlet boundary condition has been determined for the water leaving the tube side. Also, no mass leakage or permeability from the tube side to the shell side is viable.

Because of LTNE consideration, the heat flux via the void and the solid matrix of Copper wick is quite distinct. Indeed, when the interface wall faces the void area, heat flux leads to $\varepsilon q_{\mathrm{PCM}}$ or $\varepsilon q_{\mathrm{TSF}}$. However, to flux the heat from the Copper wick solid matrix, $q_{\mathrm{CW}}(1-\varepsilon)$ can be expected. So, the comprehensive heat flux equation in the interface wall is provided [45]:

$$q_{\mathrm{T,W}} = q_{\mathrm{PCM}}\varepsilon + q_{\mathrm{CW}}(1-\varepsilon) \quad (45)$$

Around the shell side, it is notable that to control the pressure gauge inside the shell, We have taken a zero-pressure reference point in the left-bottom corner of shell side [45]. Moreover, the outer surface of LHTES is thoroughly thermal insulated.

3.2. Characteristic parameters

One of the most important criteria in the current study is melting volume fraction (MVF). It can be obtained via Equation (44):

$$MVF = \frac{\iiint_V \varepsilon \varphi dV}{\iiint_V \varepsilon dV} \quad (44)$$

in the above equation, dV and V are the revolved volume element of the domain, and the revolved domain volume, respectively.

In the case of sensible aspect of the energy during phase changing is considered, Equation (45) provides it:

$$Q_{\mathrm{Sensible}} = (\rho C_P)_{\mathrm{CW}}(T - T_0)\oint_V (1-\varepsilon)dV + \left(\oint_V \left(\int_{T_0}^{T} (\rho C_P)_{\mathrm{PCM}} \varepsilon dT\right) dV\right) + (\rho C_P)_{\mathrm{Wall}} V_{\mathrm{Wall}}(T - T_0) \quad (45)$$

Latent aspect of the same energy can be calculated as below:

$$Q_{\mathrm{Latent}} = \oint_V \varepsilon L_{\mathrm{PCM}} \rho_{\mathrm{PCM}} \varphi \, dV \quad (46)$$

and finally, Equation (47) shows the stored energy as total values of latent and sensible heat:

$$Q_{\mathrm{store}} = Q_{\mathrm{Latent}} + Q_{\mathrm{Sensible}} \quad (47)$$

Power leading from the energy storage:

$$Power = \frac{Q_{\mathrm{store}}}{time} \quad (48)$$

Applying the average outlet velocity in tube side, U_{TSF}, the TSF Reynolds number is configured in Equation (49):

$$\mathrm{Re} = \frac{\rho_{\mathrm{TSF}} d_{\mathrm{inner-tube}} U_{\mathrm{TSF}}}{\eta_{\mathrm{TSF}}} \quad (49)$$

4. Numerical approach

4.1. Utilized Numerical Approach

The computational fluid dynamics (CFD) approach was initiated using the finite element method, where the governing equations were transformed into a more flexible weak form and integrated over the relevant domains [46]. Temperature and velocity fields were handled using second-order elements. Gauss quadrature integration was applied to these integrated equations across the domain elements, generating a set of algebraic equations. These equations were solved iteratively and fully coupled using the Newton method, supported by the PARDISO solver [47,48]. To enhance stability and ensure convergence, a Newton damping factor of 0.9 was employed. The phase change equations were particularly sensitive to time step sizes because the strong source terms in the momentum equations reduce velocities to zero in solidified zones. Additionally, the latent heat term in the energy equation was closely tied to time. To maintain controlled time steps and keep the solution's relative error below 10^{-4}, the backward differential formula (BDF) was used, allowing flexibility between orders 1 and 2 [49]. This automatic time-stepping approach improves solution accuracy while also reducing overall computation time by selecting optimal, stable time steps.

Moreover, to enhance solver stability and support model convergence, the dynamic viscosity of the PCM (μ_{PCM}) is deliberately adjusted. This is described by the following equation:

$$\mu_{PCM} = \varphi \mu_{PCM,liquid} + (1-\varphi)\mu_{\infty} \tag{50}$$

where μ_{∞} represents a very high viscosity value of 10^4 Pa s. With this formulation, the viscosity matches the normal dynamic viscosity, $\mu_{PCM,liquid}$, in the liquid phase (when $\varphi = 1$), while it is artificially increased in the solid phase (when $\varphi = 0$). This artificial viscosity increase plays a key role in fulfilling the purpose of the source terms, enforcing zero velocity within solid regions. By defining dynamic viscosity this way, the method not only improves solver stability and ensures smoother simulations but also preserves the physical accuracy of the model.

4.2. Grid independency process

Since the finite element method (FEM) has been applied in the present study, size of the mesh gets an effective role on the obtained results, directly. Reaching to the results by enough accuracy is also a vital process which should be done in the such problems. Thus, four variety grids have been provided to probe the suitable one in which the obtained results are fully independent. The grids are tested in the following criteria: fin aspect ratio $AR_{fin} = 3$, shell Copper wick aspect ratio $AR_{CW,\ Shell} = 7$, and inlet velocity $U_{in} = 0.1$ m/s. All the other parameters are assumed to be constant as mentioned on Fig. 1. Anyway, grid independency process has been conducted for both the melting and the solidification modes. In accordance with Fig. 2, the melting mode shows a more sensitive reaction to the grid size change; however, the solidification mode is inherently passive than any size change. Focusing on the melting mode, it can be found that from the finer to the extra fine grid size, the minimum variation has just been occurred. So, the grid with the finer mesh has been opted. Fig. 3 reveals the physical model along with the chosen grid size. To better distinguish the applied mesh, we have presented different views in details. As seen, the quadrilateral and the triangular elements have been extended in the related zones throughout the physical model. Anyway, the chosen mesh size contains 74251 domain elements and 2848 boundary elements. Mesh distribution has been divided into three distinct zones: inside Copper tube, solid wall Copper tube along with the thermal fins, and the shell side.

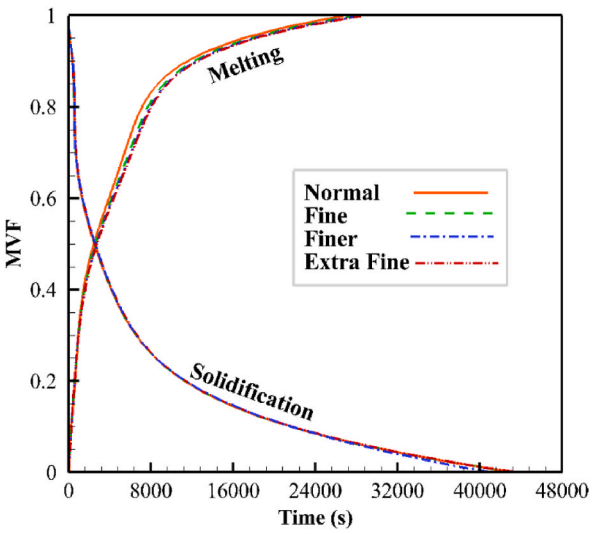

Fig. 2. Evaluation of the grid independency for melting and solidification processes.

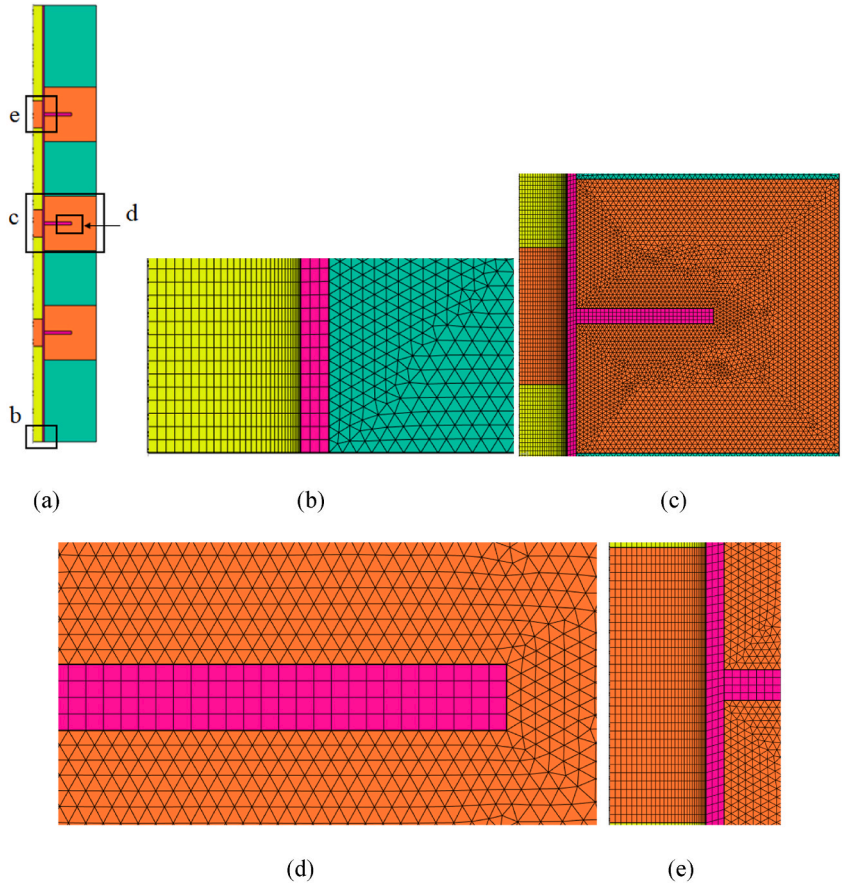

Fig. 3. (a) Overall view of the physical model in which the mesh distribution is in the hidden mode to avoid complexity, (b) focusing on the left-bottom side of the model, (c) a view of the fin as well as the metal foams extended in the shell and the tube side, (d) Mesh distribution over the fin, and (e) Mesh distributed inside the metal foam applied in the tube side.

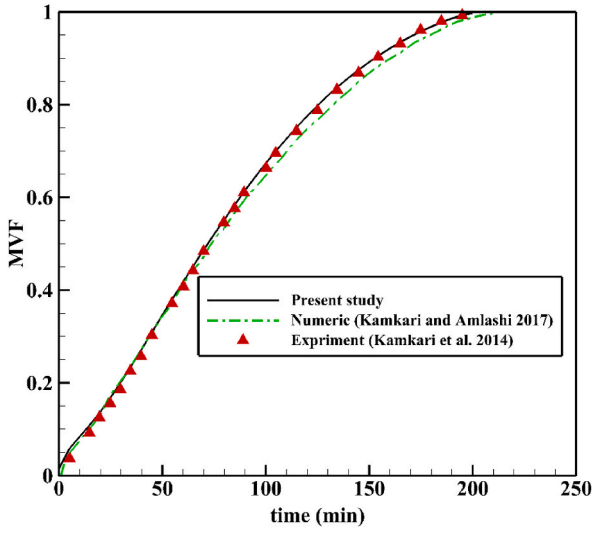

Fig. 4. The needed time to complete melting volume fraction, comparisons among present study, Kamkari and Amlashi [50] experimental work, and Kamkari et al. [51] numerical work.

Notably, in a single layer mesh size distributed inside the shell of LHTES, maximum and minimum element size have been calculated 7.53×10^{-4}, and 3.81×10^{-5}, respectively; where phase change process would be occurred. The maximum growth rate in the same area is also 1.05.

5. Code validation

To testify the accuracy of the provided numerical code in the present study, it has been compared with the valid studies which have already been published in the related field. For the first one, the comparisons are conducted among the code presented in the current study, Kamkari and Amlashi [50] Numerical study as well as Kamkari et al. [51] experimental work. The results have been depicted for the pattern of melting volume fraction of pure Lauric Acid against time in a 50cm $\times$ 120 cm test cell with respect to 70 °C vertical wall temperature. It is also assumed that the test cell has been placed on a horizontal surface. As seen in Fig. 4, the obtained pattern for the melting volume fraction has a fascinating overlap with both the numerical and the experimental results provided in Refs. [50,51].

For the second validation, the graphical results of Zheng et al. [36] work has been chosen. According to Fig. 5, contours of the melting front of pure Paraffin wax inside an enclosure reinforced by Copper metal foam have been evaluated in three different times, 1.5 h, 3 h, and 4.5 h, where the left vertical wall has been taken into account to be as hot wall while the others were fully insulated. From comparison between the first (Zheng et al. [36]) and the second rows (present code) in Fig. 5, it can be found that the current numerical code is absolutely on agreement with the obtained results provided in the referred experimental work [36].

6. Results and Discussion

Here, the main results of the present study have been configured in the form of table, graph, bar chart, contour and streamlines. Atmosphere of the current section includes the impressions of the fin aspect ratio (AR_{fin}), the Copper wick aspect ratio ($AR_{CW,\ Shell}$) and the inlet velocity (U_{in}) on the melting/solidification modes. Indeed, it can be intriguing how the mentioned geometrical aspect ratios increase or decrease phase change process. What about the effect of the inlet velocity on the processes? Generally, the purpose of the section is reaching to the best and the worst geometrical combinations. To answer the questions, Table 2 has been designed. The first five cases are assigned to the fins aspect ratio (AR_{fin}) effect. Cases 6 to 8 cover the Copper wick aspect ($AR_{CW,\ Shell}$) ratio. Impression of the inlet velocity (U_{in}) can be shown in Cases 9 to 11. Finally, to have a comprehensive comparison, Cases 12 to14 have been provided as the reference cases. Apart from Cases 9 to 11, the other introduced cases take the geometrical changes in the physical model. To avoid repetition of showing the geometrical models, once, we have depicted each geometrical model in Fig. 6, before mounting the graphical results on them. So, the current section just supports the best and the worst cases regarding the analytical results.

According to the obtained results for Cases 1 to 5, the largest value of AR_{fin} reduces melting and solidification time, significantly. Actually, Case 5 with the narrowest fins can facilitate melting and solidification processes via proper distribution of the thermal

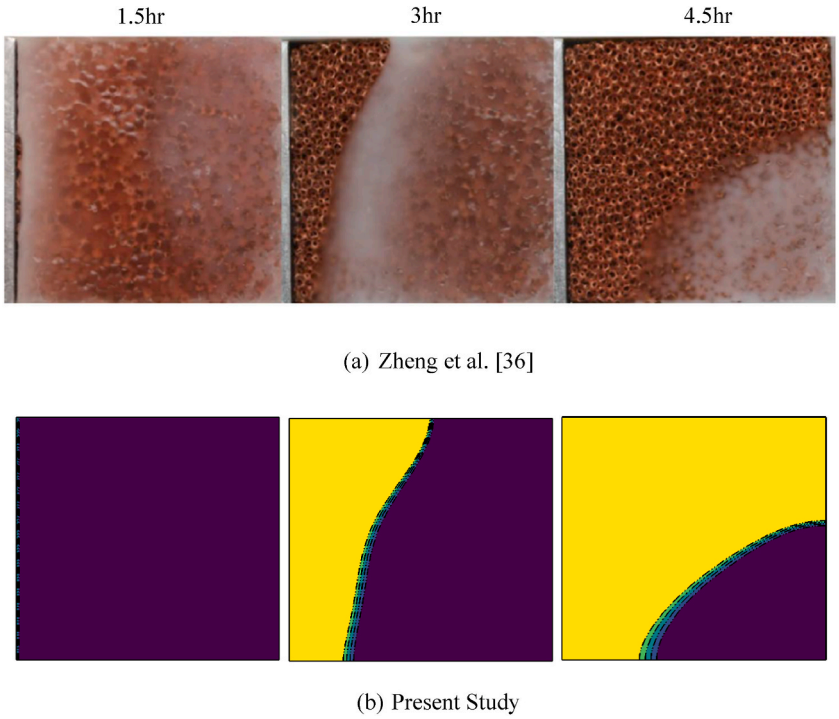

Fig. 5. Comparison the obtained results from Zheng et al. [36] work (first row) with those provided in the present study (second row).

Table 2
Probing the cases to understand the effect of each parameter (AR_{Fin}, AR_{MF} and U_{in}) leading to the identification of the best and the worst cases.

Case	Parameter	AR_{Fin}	$AR_{CW,\ Shell}$	U_{in} (m/s)	Melting time (min)	Solidification time (min)
C1	Fin Aspect Ratio	0.5	7	0.1	218	380
C2		1	7	0.1	213	377
C3		2	7	0.1	206	372
C4*		3	7	0.1	201	368
C5		4	7	0.1	198	366
C6	Copper wick Aspect Ratio	4	5.5	0.1	145	267
C7		4	6	0.1	160	307
C8		4	6.5	0.1	177	339
C9	Inlet	4	5.5	0.025	157	279
C10	Velocity	4	5.5	0.05	149	272
C11		4	5.5	0.2	144	266
C12	Reference Cases	0	0	0.1	759	954
C13		3	0	0.1	398	626
C14		0	7	0.1	217	381

C4* = The applied default values to run in the mesh independency process.

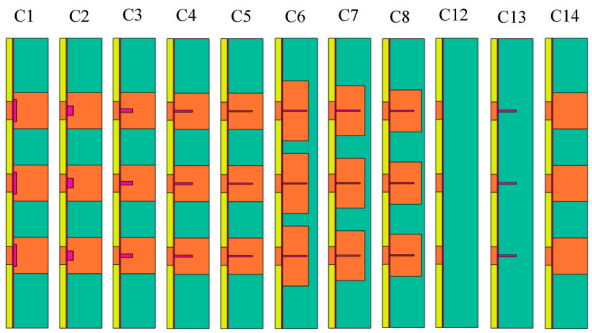

Fig. 6. The proposed geometrical combinations for the fin aspect ratio (AR_{Fin}), C1: $AR_{fin} = 0.5$, C2: $AR_{fin} = 1$, C3: $AR_{fin} = 2$, C4: $AR_{fin} = 3$, and C5: $AR_{fin} = 4$, for the metal foam aspect ratio (AR_{MF}), C6: $AR_{mf} = 5.5$, C7: $AR_{mf} = 6$, C8: $AR_{mf} = 6.5$, and three reference criteria, C12: Absence of both the thermal fins and the metal foams, C13: only the metal foams and C14: only the thermal fins.

gradients throughout the LHTES. On the contrary, Case 1 with the spread fins on the Copper tube, blocks a large portion of the thermal gradients just in vicinity of the Copper tube. Hence, the highest value of AR_{fin} is transmitted to Cases 6 to 8. The lowest value of the Copper wick aspect ratio is related to Case 6 ($AR_{CW,\ Shell} = 5.5$), where it has been spread on the Copper tube. Interestingly, the lowest needed time to complete melting/solidification of the PCM is occurred in this case. The Copper wicks spread on the Copper tube get

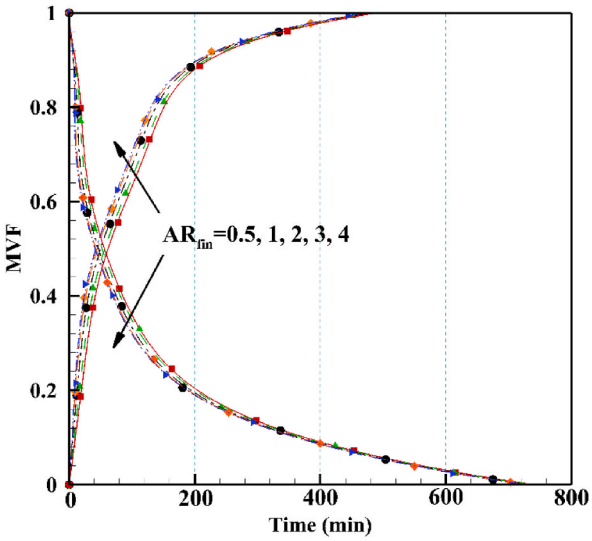

Fig. 7. Impression of the fin aspect ratio (AR_{fin}) on the melting and the solidification processes, Cases 1, 2, 3, 4, and 5.

close together and decrease the clear zones in the LHTES. In this way, joining the thermal gradients can be easier; consequently, melting/solidification front meet the center areas of LHTES in the shorter times. In contrast, when the Copper wicks touch the shell (Case 4) or reach nearby it (Case 8), the clear spaces among three Copper wicks are increased and integration of the melting (or solidification) areas is hardened. Now that the narrowest fins and the spread Copper wicks have been accomplished, Cases 9 to 11 can be discussed. Increasing the inlet velocity (U_{in}) in the Copper tube, by augmentation the thermal gradients, leads to the improved heat transfer characteristics. Thus, increasing the inlet velocity from 0.025 m/s to 0.2 m/s decreases the needed time for melting/solidification processes, slightly.

As referred cases 12 to 14 have been provided to create some comparisons among the Cases introduced in Table 2. The largest recorded times for melting/solidification processes is assigned to Case 12, where neither the thermal fins nor the Copper wicks are applied in the LHTES. Lonely, using the fins in the LHTES can improve the situation notably (see Case 13); and in an interesting comparison, absence of the thermal fins in Case 14 leads to the results provided in Case 1 which shows presence of the spread fins has not any significant difference with the absence of the thermal fins. According to the obtained comparisons, Case 6 and Case 1 introduce as the best and the worst geometrical ones in the current study, respectively.

Influences of the fin aspect ratio (AR_{fin}), Copper wick aspect ratio ($AR_{CW,\ Shell}$) as well as the inlet velocity (U_{in}) on the melting volume fraction (MVF) during phase change processes have been depicted in Figs. 7–9, respectively. As seen in all the mentioned figures, in the melting mode, the value of MVF at the initial times tends to zero; it means that the LHTES contains solid Paraffin wax. After a few seconds, the cold PCM affected by the hot crossing Water, commences to the melting with a sharp slope moving to upward. The trend is approximately kept on until about 200 min; on which, more than 80 % of the PCM gets molten. Next, the remaining solid PCM which is now far away the hot crossing Water effect, needs more time to full melting. Thus, that sharp trend transfers into a semi-plateaux one. Finally, the melting process is completed after more than 400 min. For the solidification mode, a mirror pattern can be observed than the melting mode. This time, the MVF value at the initial times is equal 1, a fully molten PCM. The cold crossing Water in the Copper tube causes Paraffin wax to become solidified. Hereon, the obtained curve trend is also divided in two parts, where the MVF value reaches 20 % by a downward sharp trend before about 200 min and then continous up to fully solidification by a semi-plateaux trend after it.

Fig. 7 shows impression of the fin aspect ratio (AR_{Fin}) on the MVF value. A longer and thinner fin, from $AR_{fin} = 0.5$ up to $AR_{fin} = 4$, by making more developed the thermal gradients inside the LHTES, leads to the shorter times for the melting and solidification processes, specially in the MVF range of 20 %–80 %. As seen, the curve regarding the longest and the thinnest fins ($AR_{fin} = 4$) has the most shift to upward and downward for the melting and the solidification modes, respectively.

The significant effectiveness of the Copper wick aspect ratio ($AR_{CW,\ Shell}$) on the MVF value can be observed in Fig. 8; where the obtained curves have gotten more distance than together. As mentioned in Table 2, a more spread Copper wick reduces the clear spaces in the LHTES and consequently, facilitates the thermal gradients integration throughout the shell. Nonetheless, a smaller value of $AR_{CW,\ Shell}$ can shorten the needed time to full melting and solidification.

Fig. 9 reveals that increasing the inlet velocity related to the Copper tube has a trivial positive effect on the melting and solidification processes. Actually, the inlet velocity gets a indirect impression on the heat transfer characteristics, the thermal gradients. Hence, just increasing the inlet velocity cannot improve the thermal gradients arousal, dramatically.

In practice, the LHTES during the melting and the solidification processes gets charging and discharging modes, respectively. Fig. 10(a) and (b) provide the stored and the released power for those 14 cases during the charging and discharging modes. It is worth to note that the bar charts in Fig. 10 have deliberately been organized to obtain in 90 % progress, a valuable percentage demonstrated

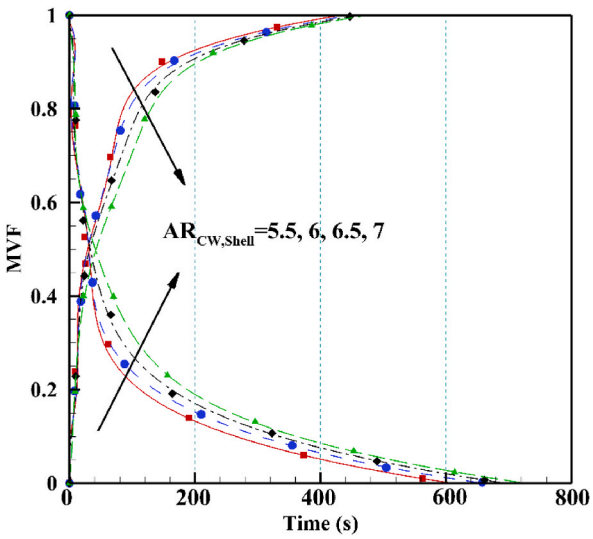

Fig. 8. Impression of the metal foam aspect ratio ($AR_{CW,\ Shell}$) on the melting and the solidification processes, Cases 5, 6, 7, and 8.

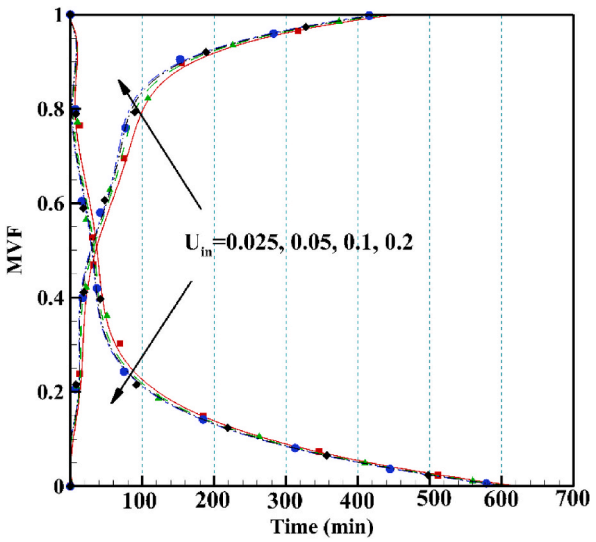

Fig. 9. Effect of the inlet velocity (U_{in}) on the melting and the solidification processes, Cases 6, 9, 10 and 11.

in each mode. In accordance with Fig. 10(a) and (b), a slight positive effect has been occurred via narrower and longer thermal fins launched inside the LHTES. Indeed, 10 % and 4 % more power can be stored and released, respectively, when utilizing Case 5 against Case 1. Despite of the smooth impression of the thermal fins on the charging/discharging power, the Copper wicks geometrical form gets significant effect inside the LHTES; so that, Case 6 than Case 8 shows an evident stored and released power improvement, about 18.5 % for charging and 21 % for discharging. Since the best geometrical case is the sixth, its power improvement percentage versus the default case, the fourth, has been calculated. Over 38 % belongs to both stored and released modes, the incredible enhancement just reached through the geometrical decisions. The best geometrical options have been launched in Cases 9 to 11 and then the pure effect of the inlet velocity (U_{in}) on the stored/released power has been shown. The most value of the charging/discharging power is provided via Case 11, where Water along with the highest inlet velocity flows in the Copper tube. Nonetheless, the obtained values for the stored and the released power via the highest velocity have a negligible eminence (only about 1.5 % and 1 %) than that of Case 6, the best geometrical design. About the reference cases, it should be said that Cases 12 and 13 are not practically comparative against the others due to the low value of charging/discharging power obtained by them. One is empty of the geometrical options (Absence of the thermal fins and the Copper wicks) and another has just the thermal fins. As already referred, Cases 1 and 14 are in the same level. Hence, the reached stored/released power for both of them is approximately equal, more than 27w in charging mode and 15.7w in discharging one. Actually, presence of the spread thermal fins on the Copper tube (Case 1) than the absence of them (Case 14) has not any significant impression on the charging/discharging power. Thus, the optimum geometrical model for reaching to the affordable aspects should be considered as well.

In this part of Results and Discussion section, the melting front, the streamlines and the temperature distribution of the best and the worst cases, Cases 6 and 1, have been covered in the set of Figs. 11 and 12. The results are shown in five different times, 15 min, 30 min, 60 min, 90 min and 120 min.

The set of Fig. 11(a) are assigned to the melting mode of Case 6. The progress of the melting front from a time to another has been shown, where the melting process is started inside the Copper wicks around the thermal fins and developed to the other clear areas. The molten areas include the streamlines. Compression and expansion streamlines in the initial times to the last times are depicted in the five left figures in Fig. 11(a). Inevitably, the solid areas are empty of any molten PCM; So, no streamlines are found in there. The temperature distribution is organized in the five right figures in Fig. 11(a). The heat transfers from the hot crossing Water within the tube side to the various areas of the shell. Definitely, because of the high thermal conductivity of the Copper wicks and the thermal fins, the temperature distribution in these areas is more than the other ones. Adapted with those shown for the melting front and the streamlines, wherever the PCM is molten, high temperature is dominant. In contrast, the area containing the solid PCM are still cold. According to the obtained results in Fig. 11(b), the cold crossing Water transmits the low temperature to the Copper wicks, the thermal fins and the clear areas of the shell. On behalf of the reasons mentioned for the set of Fig. 11(a), it is expected that the cold transfers into the shell very well since We have encountered the best case. Fig. 11(b) show the melting front has a suitable progress; the streamlines due to the solidification are gradually vanished and finally, the low temperature conquers almost overall areas of the LHTES.

Fig. 12 (a) and (b) have been presented to show the weakness of Case 1 design in the melting front progress, the streamlines and the temperature distribution, both in the melting mode and the solidification one. As seen, the thermal fins are spread on the Copper tube. In addition, the largest spaces have been created among the Copper wicks. These two bad tastes in the design phase are enough for an improper melting front progress and the compression streamlines even in the developed times. Accordingly, the portion of solid areas in the last time is still much. Moreover, the streamlines in an unexpected situation have faded in some molten areas (see five left figures in Fig. 12(a)). To find the reason, five right figures in Fig. 12(a) have been depicted. Despite of the fact that the heat has been

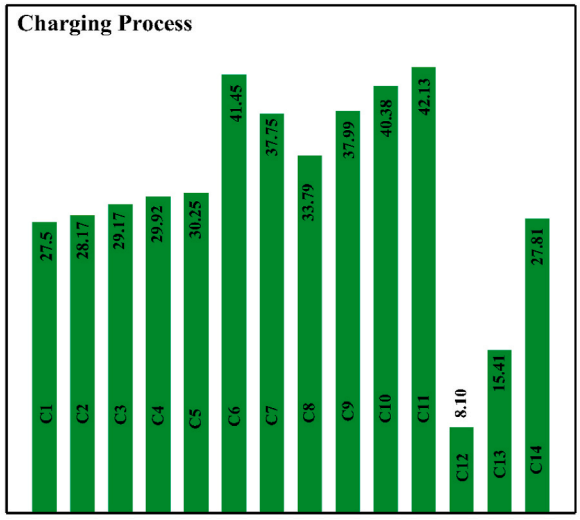

(a)

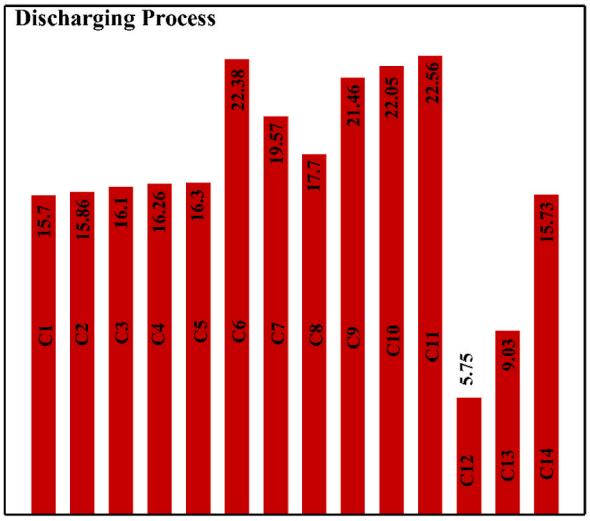

(b)

Fig. 10. Calculated power (W) in (a) Charging process at 90 % melting volume fraction, and (b) Discharging process at 10 % melting volume fraction.

transferred into the Copper wicks, due to the geometrical conditions, it has almost remained inside the mentioned areas with a low power to distribute in the clear areas. It causes the thermal equilibrium to be dominant in those molten areas; hence, there has not been any thermal gradients in there and consequently, no molten PCM circulation is expected in the referred areas. The same situations have also been happened in the solidification mode as shown in Fig. 12(b). Disability in the melting front progress, the weak streamlines, and lack of the thermal gradients can be observed in the solidification mode; where all of them have been occurred because of the geometrical design in Case 1, the worst case.

7. Conclusion and remarks

The FEM was applied to simulate a shell and tube LHTES under different geometric and parametric options in the form of 14 cases. The LHTES was contained the thermal disk fins reinforced by the sintered Copper wicks. Keeping the constant volumes of the thermal

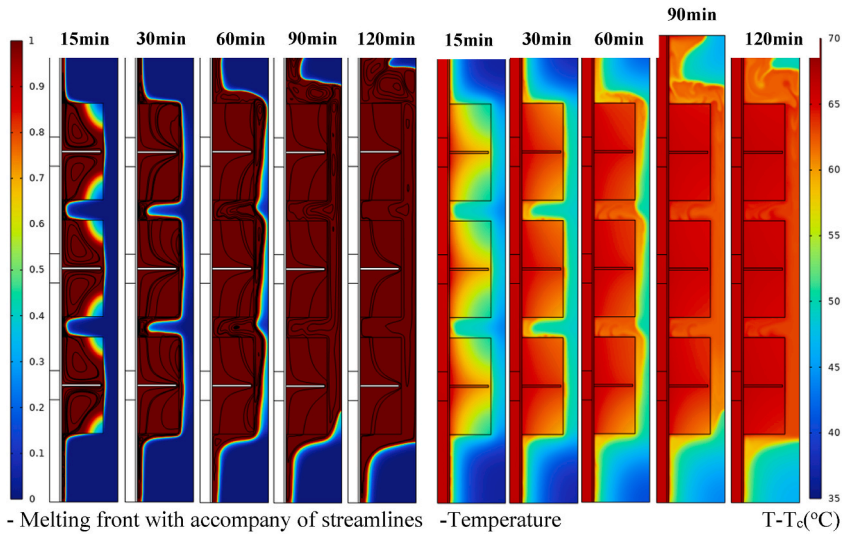

Fig. 11. The best geometrical combination for the thermal fins and the Copper wicks in the (a) Melting mode, and (b) Solidification mode.

fins and the Copper wicks, the best and the worst cases were chased step by step. The most substantial results have been provided as below:

I) A narrower and longer fin provides the better thermal properties throughout the LHTES; however, the obtained results show a slight enhancement percentage, lower than 2 %, reached via the fin geometrical variations. In addition, presence of the thermal fins spread on the exterior surface of the Copper tube does not make any change than absence of them.

II) After determination the best option of the fin, effect of the sintered Copper wicks inside the LHTES was probed. This time, the Copper wicks spread on the exterior surface of the Copper tube along with the narrowest and the longest fins revealed the best geometrical case, Case 6; So that, against Case 4 (the default case), over 38 % the power improvement percentage (case 6 than default case) during the charging and the discharging modes was recorded.

III) The inlet velocity was evaluated for the optimum geometrical case introduced in the current study. As a predictable factor, increasing the inlet velocity via augmentation the fluid flow as well as thermal gradients leads to a further stored/released power.

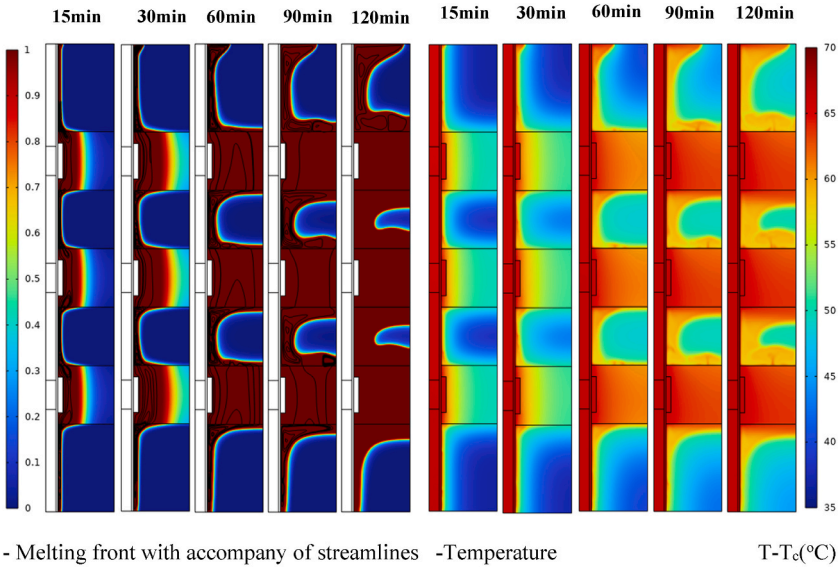

(a) Melting mode

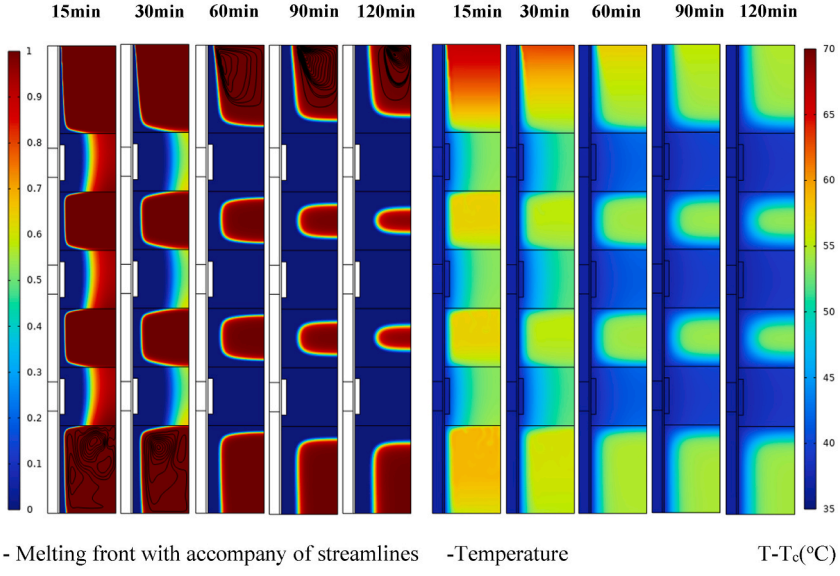

(b) Solidification mode

Fig. 12. The worst geometrical combination for the thermal fins and the Copper wicks in (a) the melting mode, and (b) the solidification mode.

CRediT authorship contribution statement

Maher Jebali: Writing – original draft, Visualization, Methodology, Investigation, Formal analysis, Conceptualization. **Khalil Hajlaoui:** Writing – review & editing, Writing – original draft, Visualization, Software, Resources, Formal analysis, Data curation. **Mohamed Bouzidi:** Writing – original draft, Visualization, Resources, Project administration, Methodology, Formal analysis. **Mansour Mohamed:** Writing – review & editing, Writing – original draft, Methodology, Formal analysis, Data curation. **Wahiba Yaïci:** Writing – review & editing, Writing – original draft, Resources, Methodology, Investigation, Formal analysis, Conceptualization. **Nashmi H. Alrasheedi:** Writing – review & editing, Writing – original draft, Project administration, Formal analysis, Data curation, Conceptualization. **Mohammad Ghalambaz:** Writing – review & editing, Writing – original draft, Visualization, Validation, Supervision, Software, Conceptualization. **Pouyan Talebizadehsardari:** Writing – review & editing, Writing – original draft, Visualization, Validation, Software, Resources, Methodology, Investigation.

Funding

This work was supported and funded by the Deanship of Scientific Research at Imam Mohammad Ibn Saud Islamic University (IMSIU) (grant number IMSIU-DDRSP-RP25).

Declaration of competing interest

The authors clarify that there is no conflict of interest for report.

Appendix A

In this section, we have shown how the calculated volumes for the fins and Copper wick have remained in their constant values, while various dimensions are applied for the thickness and the height of them. To find the values of the volumes, firstly, a manual calculation was applied for the default geometrical formation as shown in Fig. 1. Hereon, the calculation regarding the fin is extended. It is known that the thickness and the height of the fin are $t_{fin} = 2.1167$ mm and $H_{fin} = 19.05$ mm, respectively. In addition, $R_{Tube\text{-}out} = R_{Tube\text{-}in} + Tube_{wall} = 0.0066929 + 0.0012446 = 0.0079375$ mm. Now, based on the below relation, the fin volume can manually be calculated:

$$V_{fin} = \pi\left(\left(R_{Tube-out} + H_{fin}\right)^2 - R_{Tube-out}^2\right)t_{fin} \tag{A1}$$

The obtained fin volume is equal $V_{fin} = 4.42\ cm^3$. The approach to calculate the fin volume can be repeated for the Copper wick volume. It is just necessary to say that the pure volume of Copper wick can be reached by subtracting the fin volume. The relation is demonstrated as follow:

$$V_{CW,Shell} = \left(\pi\left(\left(R_{Tube-out} + W_{CW,Shell}\right)^2 - R_{Tube-out}^2\right)H_{CW}\right) - V_{fin} \tag{A2}$$

Anyway, after calculation, the Copper wick volume is also equal $V_{CW} = 224.53\ cm^3$. In the next step, we have defined two aspect ratios (AR); one for the fin and another for Copper wick porous medium. To do it, Eq. (A3) have been given by

$$AR_{fin} = \frac{H_{fin}}{R_{Tube-Nominal}}, AR_{CW,Shell} = \frac{W_{CW,Shell}}{R_{Tube-Nominal}} \tag{A3}$$

Applying Eq. (A3) in Eqs. (A1) and (A2):

$$V_{fin} = \pi\left(\left(R_{Tube-out} + AR_{fin}R_{Tube-Nominal}\right)^2 - R_{Tube-out}^2\right)t_{fin} \tag{A4}$$

$$V_{CW,Shell} = \left(\pi\left(\left(R_{Tube-out} + AR_{CW}R_{Tube-Nominal}\right)^2 - R_{Tube-out}^2\right)H_{CW}\right) - V_{fin} \tag{A5}$$

According to the contracted constraints, constant values for the volumes and the outer radius of tube ($R_{Tube\text{-}Nominal}$), as well as the control parameters, AR_{fin} and AR_{CW}, the only variable parameters to keep constant the volumes can be related to the fin thickness and the Copper wick height. Then,

$$t_{fin} = \frac{V_{fin}}{\pi\left(\left(R_{Tube-out} + AR_{fin}R_{Tube-Nominal}\right)^2 - R_{Tube-out}^2\right)} \tag{A6}$$

$$H_{CW} = \frac{V_{CW,Shell} + V_{fin}}{\pi\left(\left(R_{Tube-out} + AR_{CW}R_{Tube-Nominal}\right)^2 - R_{Tube-out}^2\right)} \tag{A7}$$

Finally, Eqs. (A6) and (A7) are only controlled via AR_{fin} and AR_{CW}. While, changes in the model geometry can be possible without any variation in the both volumes.

Data availability

Data will be made available on request.

References

[1] A. Afzal, A.M. Samee, R.A. Razak, M. Ramis, Steady and transient state analyses on conjugate laminar forced convection heat transfer, Arch. Comput. Methods Eng. 27 (1) (2020) 135–170.
[2] M. Gholami, M.R. Nazari, M.H. Talebi, F. Pourfattah, O.A. Akbari, D. Toghraie, Natural convection heat transfer enhancement of different nanofluids by adding dimple fins on a vertical channel wall, Chin. J. Chem. Eng. 28 (3) (2020) 643–659.
[3] H. Sajjadi, A.A. Delouei, R. Mohebbi, M. Izadi, S. Succi, Natural convection heat transfer in a porous cavity with sinusoidal temperature distribution using Cu/water nanofluid: double MRT lattice Boltzmann method, Commun. Comput. Phys. 29 (1) (2021) 292–318.

[4] J. Liu, P. Yu, Y. Li, C. Wan, D. Du, Numerical simulation on convective heat transfer characteristics in porous media based on the digital rock technology, Int. J. Heat Mass Tran. 196 (2022) 123323.
[5] K. Anand, A. Bhardwaj, S. Chaudhuri, V.K. Mishra, Self-organizing map network for the decision making in combined mode conduction-radiation heat transfer in porous medium, Arabian J. Sci. Eng. 47 (12) (2022) 15175–15194.
[6] S. Chen, W. Gong, Y. Yan, Conjugate natural convection heat transfer in an open-ended square cavity partially filled with porous media, Int. J. Heat Mass Tran. 124 (2018) 368–380.
[7] S. Mehryan, M. Ismael, M. Ghalambaz, Local thermal nonequilibrium conjugate natural convection of nano-encapsulated phase change particles in a partially porous enclosure, Math. Methods Appl. Sci. (2020).
[8] P.H. Jadhav, N. Gnanasekaran, D. Arumuga Perumal, Numerical consideration of LTNE and darcy extended forchheimer models for the analysis of forced convection in a horizontal pipe in the presence of metal foam, J. Heat Tran. 143 (1) (2021) 012702.
[9] L.-C. Cheng, S.-C. Wong, Pore-scale numerical simulation and LTNE analysis for fully-developed forced convective heat transfer in packed beds of mono-sized rough spheres covering near-wall and core regions, Int. J. Heat Mass Tran. 208 (2023) 124047.
[10] H. Esmonde, Fractal and fractional derivative modelling of material phase change, Fractal Fractional 4 (3) (2020) 46.
[11] M. Arıcı, Ç. Yıldız, S. Nižetić, A. Shahsavar, A. Campo, Implications of boundary conditions on natural convective heat transfer of molten phase change material inside enclosures, Int. J. Energy Res. 45 (5) (2021) 7631–7650.
[12] A. Kumar, A. Saxena, S. Pandey, A. Gupta, Cooking performance assessment of a phase change material integrated hot box cooker, Environ. Sci. Pollut. Control Ser. 31 (53) (2024) 62392–62407.
[13] Y.-M. Chu, D. Yadav, A. Shafee, Z. Li, Q.-V. Bach, Influence of wavy enclosure and nanoparticles on heat release rate of PCM considering numerical study, J. Mol. Liq. 319 (2020) 114121.
[14] A. Memon, G. Mishra, A.K. Gupta, Buoyancy-driven melting and heat transfer around a horizontal cylinder in square enclosure filled with phase change material, Appl. Therm. Eng. 181 (2020) 115990.
[15] A. Labihi, F. Aitlahbib, H. Chehouani, B. Benhamou, M. Ouikhalfan, C. Croitoru, I. Nastase, Effect of phase change material wall on natural convection heat transfer inside an air filled enclosure, Appl. Therm. Eng. 126 (2017) 305–314.
[16] M. Boujelbene, S.A. Mehryan, M. Sheremet, M. Shahabadi, N.B. Elbashir, M. Ghalambaz, Numerical study of a Non-Newtonian phase change flow in finned rectangular enclosures, Facta Universitatis, Series: Mech. Eng. (2024).
[17] M.E. Zayed, J. Zhao, W. Li, A.H. Elsheikh, A.M. Elbanna, L. Jing, A. Geweda, Recent progress in phase change materials storage containers: geometries, design considerations and heat transfer improvement methods, J. Energy Storage 30 (2020) 101341.
[18] L.-L. Tian, X. Liu, S. Chen, Z.-G. Shen, Effect of fin material on PCM melting in a rectangular enclosure, Appl. Therm. Eng. 167 (2020) 114764.
[19] R. Kalbasi, M. Afrand, J. Alsarraf, M.-D. Tran, Studies on optimum fins number in PCM-based heat sinks, Energy 171 (2019) 1088–1099.
[20] M. Gürtürk, B. Kok, A new approach in the design of heat transfer fin for melting and solidification of PCM, Int. J. Heat Mass Tran. 153 (2020) 119671.
[21] B. Kok, Examining effects of special heat transfer fins designed for the melting process of PCM and Nano-PCM, Appl. Therm. Eng. 170 (2020) 114989.
[22] M. Ghalambaz, J. Zhang, Conjugate solid-liquid phase change heat transfer in heatsink filled with phase change material-metal foam, Int. J. Heat Mass Tran. 146 (2020) 118832.
[23] S.-B. Chen, S. Saleem, M.N. Alghamdi, K.S. Nisar, A. Arsalanloo, A. Issakhov, W.-F. Xia, Combined effect of using porous media and nano-particle on melting performance of PCM filled enclosure with triangular double fins, Case Stud. Therm. Eng. 25 (2021) 100939.
[24] A. NematpourKeshteli, M. Iasiello, G. Langella, N. Bianco, Enhancing PCMs thermal conductivity: a comparison among porous metal foams, nanoparticles and finned surfaces in triplex tube heat exchangers, Appl. Therm. Eng. 212 (2022) 118623.
[25] A. Khanlari, İ. Aytaç, A.D. Tuncer, H.İ. Variyenli, H.N. Şahin, Improving the performance of a PCM integrated solar air collector by adding porous fins over the bottom side of the absorber: a transient CFD study, J. Energy Storage 90 (2024) 111847.
[26] N.K.G. Ranga, S.K. Gugulothu, P. Gandhi, Thermal optimization of latent heat energy storage through Fin geometry natural convection and PCM properties for superior phase change performance, Heat Transfer (2025).
[27] Y. Cao, H. Ayed, A. Algelany, M. Dahari, P.Q.P. Nguyen, K.A. Gepreel, V.N. Nguyen, M. Ehab, M. Wae-hayee, Receiving heat from a PCM tank by using natural convection of water and NEPCM: a simulation for LHTES application, Case Stud. Therm. Eng. 35 (2022) 102123.
[28] J. Pássaro, A. Rebola, L. Coelho, J. Conde, G. Evangelakis, C. Prouskas, D. Papageorgiou, A. Zisopoulou, I. Lagaris, Effect of fins and nanoparticles in the discharge performance of PCM thermal storage system with a multi pass finned tube heat exchange, Appl. Therm. Eng. 212 (2022) 118569.
[29] Y. Amini, F. Hekmat, Improving the thermal performance of a spherical latent thermal energy storage using innovative fins and porous media, Phys. Fluids 37 (1) (2025).
[30] A. Jaberi, S. Hossainpour, A. Kiyoumarsioskouei, The impact of utilizing porous fins on the performance of PCM melting process in a horizontal Latent Heat Thermal energy storage, J. Energy Storage 97 (2024) 112893.
[31] M. Mozaffari, K. Hajlaoui, O. Younis, A. Ahmed, D.M. Khidhir, A. Hajjar, M. Ghalambaz, N.H. Alrasheedi, Thermal performance and melting behavior of partially funnel-shaped anisotropic copper Foam/Paraffin PCM within an LHTES, Heat Transfer (2025).
[32] A.I.N. Korti, H. Guellil, Experimental study of the effect of inclination angle on the paraffin melting process in a square cavity, J. Energy Storage 32 (2020) 101726.
[33] A. Agarwal, R. Sarviya, Characterization of commercial grade paraffin wax as latent heat storage material for solar dryers, Mater. Today Proc. 4 (2) (2017) 779–789.
[34] N. Ukrainczyk, S. Kurajica, J. Šipušić, Thermophysical comparison of five commercial paraffin waxes as latent heat storage materials, Chem. Biochem. Eng. Q. 24 (2) (2010) 129–137.
[35] S.-K. Choi, S.-O. Kim, T.-H. Lee, Dohee-Hahn, Computation of the natural convection of nanofluid in a square cavity with homogeneous and nonhomogeneous models, Numer. Heat Transf. A Appl. 65 (4) (2014) 287–301.
[36] H. Zheng, C. Wang, Q. Liu, Z. Tian, X. Fan, Thermal performance of copper foam/paraffin composite phase change material, Energy Convers. Manag. 157 (2018) 372–381.
[37] Y. Yao, H. Wu, Macroscale modeling of solid–liquid phase change in metal foam/paraffin composite: effects of paraffin density treatment, thermal dispersion, and interstitial heat transfer, J. Therm. Sci. Eng. Appl. 13 (4) (2021) 041024.
[38] S. Zhang, Y. Yao, Y. Jin, Z. Shang, Y. Yan, Heat transfer characteristics of ceramic foam/molten salt composite phase change material (CPCM) for medium-temperature thermal energy storage, Int. J. Heat Mass Tran. 196 (2022) 123262.
[39] Y. Yao, H. Wu, Interfacial heat transfer in metal foam porous media (MFPM) under steady thermal conduction condition and extension of Lemlich foam conductivity theory, Int. J. Heat Mass Tran. 169 (2021) 120974.
[40] X. Yang, P. Wei, X. Wang, Y.-L. He, Gradient design of pore parameters on the melting process in a thermal energy storage unit filled with open-cell metal foam, Appl. Energy 268 (2020) 115019.
[41] V. Joshi, M.K. Rathod, Thermal transport augmentation in latent heat thermal energy storage system by partially filled metal foam: a novel configuration, J. Energy Storage 22 (2019) 270–282.
[42] V.V. Calmidi, R.L. Mahajan, Forced convection in high porosity metal foams, J. Heat Tran. 122 (3) (2000) 557–565.
[43] Y. Yao, H. Wu, Z. Liu, Direct simulation of interstitial heat transfer coefficient between paraffin and high porosity open-cell metal foam, J. Heat Tran. 140 (3) (2018).
[44] Z. Liu, Y. Yao, H. Wu, Numerical modeling for solid–liquid phase change phenomena in porous media: Shell-and-tube type latent heat thermal energy storage, Appl. Energy 112 (2013) 1222–1232.
[45] J. Shafi, M. Ghalambaz, M. Fteiti, M. Ismael, M. Ghalambaz, Computational modeling of latent heat thermal energy storage in a shell-tube unit: using neural networks and anisotropic metal foam, Mathematics 10 (24) (2022) 4774.

[46] O. Zienkiewicz, R. Taylor, P. Nithiarasu, Chapter 3-the characteristic-based split (CBS) algorithm: a general procedure for compressible and incompressible flow. The Finite Element Method for Fluid Dynamics, seventh ed., Butterworth-Heinemann, Oxford, 2014, pp. 87–125.
[47] M. Bollhöfer, O. Schenk, R. Janalik, S. Hamm, K. Gullapalli, State-of-the-art sparse direct solvers. Parallel Algorithms in Computational Science and Engineering, 2020, pp. 3–33.
[48] M. Bollhofer, A. Eftekhari, S. Scheidegger, O. Schenk, Large-scale sparse inverse covariance matrix estimation, SIAM J. Sci. Comput. 41 (1) (2019) A380–A401.
[49] G. Söderlind, L. Wang, Adaptive time-stepping and computational stability, J. Comput. Appl. Math. 185 (2) (2006) 225–243.
[50] B. Kamkari, H.J. Amlashi, Numerical simulation and experimental verification of constrained melting of phase change material in inclined rectangular enclosures, Int. Commun. Heat Mass Tran. 88 (2017) 211–219.
[51] B. Kamkari, H. Shokouhmand, F. Bruno, Experimental investigation of the effect of inclination angle on convection-driven melting of phase change material in a rectangular enclosure, Int. J. Heat Mass Tran. 72 (2014) 186–200.